

## Crashworthiness behaviour of the stiffened panel in idealized penetration test: A developed stiffening configuration against impact loading



Brilliant Aditya Fhandy<sup>1</sup>, Aditya Rio Prabowo<sup>1</sup>, Tuswan Tuswan<sup>2,\*</sup>, Achmad Zubaydi<sup>3</sup>, Dharu Feby Smaradhana<sup>4</sup>, Seung Jun Baek<sup>5</sup>, Siti Nurlita Fitri<sup>6</sup>

<sup>1</sup> Department of Mechanical Engineering, Universitas Sebelas Maret, Surakarta, Indonesia

<sup>2</sup> Department of Naval Architecture, Universitas Diponegoro, Semarang, Indonesia

<sup>3</sup> Department of Naval Architecture, Institut Teknologi Sepuluh Nopember, Surabaya, Indonesia

<sup>4</sup> Department of Aeronautics, Imperial College London, London, United Kingdom

<sup>5</sup> Advanced-Green Technology Center, Korea Marine Equipment Research Institute, Busan, South Korea

<sup>6</sup> Department of Civil Engineering, Gifu University, Gifu, Japan

### ARTICLE INFO

Keywords:

Engineering

Crashworthiness behaviour

Penetration test

Steel panel

Stiffening system

### ABSTRACT

This study focuses on the crashworthiness performance due to collision accidents on stiffened plate panels on ship structures. Numerical impact simulation using explicit dynamic with ANSYS software on the stiffened plate with quasi-static loading is investigated. The investigation emphasizes numerical parameters such as mesh size and geometric parameters, including stiffener type, spacing, and configuration. Benchmarking results show high accuracy, with force-displacement trends and fracture energy discrepancies less than 5 % compared to experimental data. Deformation and fracture contours are similar to experimental observations, particularly at plate-stiffener intersections. Key findings highlight the crucial impact of mesh size on accuracy, where a finer mesh size significantly increases the accuracy level. The study also evaluates the effect of different stiffener types, configurations, and spacings on crashworthiness. The Single-L and Cross-Y stiffeners perform better than the T and I stiffeners. Other investigations show stiffener configuration and stiffener spacing generally influence crashworthiness performance. This research underlines the importance of detailed structural analysis for enhancing ship safety in collision scenarios, vital for minimizing potential losses and environmental damage.

### 1. Introduction

Marine transportation is essential in the global economy, with nearly 90 % transported by sea [1,2]. Disaster prevention efforts at sea have been made amid the rapid development of marine transportation, but the accident rate in the marine transportation industry is still high [3]. Marine transportation safety has become a central focus of the global marine transportation industry despite being less developed than land and air transportation safety research. This research is crucial due to the potential for accidents and significant losses. It systematically and in-depth explores the mechanisms and causes of marine accidents, predicts potential

\* Corresponding author.

E-mail address: [tuswan@lecturer.undip.ac.id](mailto:tuswan@lecturer.undip.ac.id)

consequences, analyzes accident probability distributions, devises prevention strategies, and examines the relationship between causal factors and the severity of damage [4].

Identifying factors contributing to marine transportation accidents is critical for minimizing their occurrence and improving safety. These factors encompass human error, traffic conditions, weather conditions, and mechanical failures. The International Maritime Organization (IMO) categorizes marine transportation accidents into eight types: shipwreck, grounding, hull equipment failure, contact, fire, collision, war damage, and oil spills. Such accidents can lead to substantial economic losses, environmental damage, and loss of life [5]. IMO uses a structured Formal Safety Assessment (FSA) to evaluate the risk of accidents in maritime transportation through the Maritime Safety Committee (MSC) [3].

Analysis of marine transportation accidents indicates that groundings and ship collisions are the most prevalent globally. With 90 % of international trade transported by sea, congestion in local waterways and ports heightens the risk of collisions [6]. Collisions can result in structural damage to ships, oil spills, environmental harm, explosions, route congestion, permanent vessel damage, and loss of life. Given these potential losses, research into collision safety is crucial [7,8]. The marine transportation industry prioritizes crashworthiness to enhance hull structure performance, focusing on the hull's ability to absorb impact through plastic deformation, thereby minimizing mechanical damage and improving survival chances during collisions [9,10,11]. Crashworthiness research focuses on the structure's ability to absorb energy post-collision [12]. This research often involves experiments that replicate the actual structural construction of ships to gather reliable data. The data from these experiments serve as a benchmark to validate numerical or analytical approaches to studying structural responses to ship collisions [13]. However, experimental research faces challenges such as variability in material characteristics, defining failure criteria, distortions during the construction and assembly of structural models, maintaining structural integrity, and accounting for hydrodynamic effects, which add significant complexity [7].

With advancements in computer technology, these complexities are increasingly managed through numerical finite element analysis (FEA). FEA allows for detailed, cost-effective research, particularly in ship structure analysis [14]. It enables the simulation of structural responses and assessment of accident worthiness in collision scenarios. In FEA, fractures are modeled by removing elements that exhibit excessive strain, highlighting how mesh size in FEA significantly influences the outcomes [15,16].

This study focuses on enhancing the design of ship hull structures to better withstand impact loading, particularly in collision scenarios, by optimizing stiffener configurations. It highlights the critical role of stiffeners in increasing the safety, reliability, and sustainability of ship structures under impact loads. Employing a comprehensive approach, the research combines numerical simulations of quasi-static impact events with extensive experimental validation to refine both numerical and physical aspects of crashworthiness design. Key numerical factors like mesh size and element quality were carefully adjusted to optimize simulation accuracy and efficiency. Additionally, the study rigorously analyzed physical characteristics such as types of stiffeners, stiffener spacing, and geometric configurations to understand their impact on energy absorption and deformation patterns. This research advances current knowledge by integrating advanced simulation tools with experimental data to develop innovative stiffening solutions.

## 2. Literature review

Research on the phenomenon of ship collision has been conducted using both experimental and numerical methods. The study aims to determine the durability of the ship structure when a ship collision incident occurs. Alsos et al. [17] used the experimental method of penetrating the stiffened plate panel to determine the damage to the ship structure due to ship collision and ship grounding incidents. The research focuses on plastic deformation and fracture in the structure. Alsos et al. [15] Then, they continued their research using numerical methods, namely the finite element method, by conducting numerical simulations of the experiments that had been carried out. The study produced numerical simulation data that focused on fracture prediction, which was then compared with experimental data that had been carried out. The experiments and simulations conducted by Alsos et al. were both conducted under quasi-static conditions.

Moreover, Abubakar et al. [16] compared experimental data on stiffened plate panel penetration by Alsos et al. [17] with simulation tests conducted using the finite element method, which focused on predicting damage to the stiffened plate panel due to penetration loads. The simulation test examined the damage to the ship's double bottom structure during a grounding incident. Paik et al. [18] aimed to develop a simulation model using the finite element method to analyze structural crashworthiness in ship collisions and grounding incidents. Their research defines key aspects such as mesh size, material stress-strain relationships, critical fracture strains, and dynamic effects. Additionally, Kõrgesaar et al. [19] discussed the benefits and disadvantages of each fracture criterion by presenting ship collision simulations that included consideration of several failure criteria utilizing various mesh densities and material models. Kõrgesaar & Romanoff [20] examined the effects of mesh size, stress triaxiality, and damage-induced softening on the ductile fracture behaviour of large-scale shell structures under multi-axial stretching. Two structural configurations were analyzed: stiffened and unstiffened panels. The comparison between numerical simulations and experimental data indicates that the simulations accurately reproduce key experimental observations, particularly with varying mesh densities. Moreover, the impact phenomenon in ship side-shell structure and single-sided stiffened and double-skinned steel sandwich panels by using numerical simulation can be found in [21,22].

Based on the above-mentioned literature, investigating the crashworthiness of stiffened plate panels in ship structures is critical, given the significant consequences of collision accidents. The impact performance of stiffener configuration on the structural integrity of a ship during a collision is influenced by several factors, including stiffener design and configuration. By optimizing the shape, type, and placement of stiffeners, ship designers can significantly improve the crashworthiness and safety of vessels. This research uses explicit dynamic numerical impact simulation with ANSYS software to evaluate the quasi-static loading on stiffened plates, emphasizing critical numerical parameters such as mesh size and geometric factors, including stiffener type, spacing, and configuration. The study of design configurations of stiffened plate panels under impact loads such as collisions is limited and crucial for maritime vessels' safety and structural integrity. These panels are pivotal in maintaining a ship's integrity by effectively absorbing energy and containing damage during high-stress collisions. Optimizing these configurations enhances a ship's resilience to impacts, preventing catastrophic failures like hull breaches and hazardous material spills. Factors such as material selection, stiffener type and configuration, and geometric optimization are rigorously analyzed and complemented by advanced numerical simulations. By advancing our understanding and implementing optimized stiffened plate panels, this research directly contributes to mitigating these risks, underscoring the urgent need for continued and focused study in this area.

## 2.1 Review of ship collision phenomenon

Impact loads can be described as high-strength loads applied over a short period. Structures subjected to impact loads are vulnerable to failure since they are typically designed to endure energy and loads incrementally [23,24]. It highlights the adverse effects of impact load phenomena, which are closely associated with damage and loss of life. Impact load phenomena can manifest in various forms, particularly in the marine industry, with ship collisions being a prime example [25].

The origin of ship collisions can be traced to sudden and generally accidental contact. Therefore, the incident can be classified as accidental loads. Due to its unintentional nature, ship collision scenarios can vary depending on several factors [26-28]. Firstly, the nature of the collision itself is significant, whether it involves a rigid body, an offshore platform, or another vessel. The forces at play during the collision are crucial, including the speed, displacement, bow structure, draft of the vessel, and the relative azimuth between the colliding ships. Additionally, the condition of the vessel colliding, such as its displacement, draft, speed, and relative azimuth, plays a role. Environmental factors like wind, waves, and current flows also contribute to the likelihood and severity of a collision. Finally, the structural capacity of the ship to withstand the impact is a critical consideration in the outcome of such incidents.

Ship collisions can involve various objects, including other ships, containers, docks, and objects that could lead to a crash [27]. In ship-to-ship collisions, the vessels are categorized as either the "struck ship," which is the vessel that is hit, or the "striking ship," which is the vessel that causes the collision [29].

The extent of damage varies depending on whether the collision occurs near the main or center decks and the specific area of impact, whether it be the fore, mid, or aft sections, since these areas have different structural shapes and patterns [27].

The ship collision phenomenon is divided into two primary components: external dynamics and internal mechanics. The external dynamics concern the motion of the vessels and their interaction with surrounding conditions, while the internal mechanics focus on the material damage to the structures involved in the collision [30]. Critical parameters for external dynamics include the mass or type of ship, collision speed, collision location, and collision angle, which can be used to verify the structural response in the internal mechanics of the collision. Several calculation methods exist to estimate the structural response in a ship collision, such as the empirical methods introduced by Minorsky (1958) in Eq. 1, Vaughan (1978) in Eq. 2, Woisin (1979) in Eq. 3, and Paik (1994) in Eq. 4 [27]:

$$E = 47.2 R_T + 32.7 \quad (1)$$

$$E = 93 R_T + 33 A \quad (2)$$

$$E = 47.2 R_T + 0.5 \Sigma (h t_s^2) \quad (3)$$

$$E = C_{1.5} \sigma_0 l^{1.5} t_{eq}^{1.5} \quad (4)$$

where  $E$  is the energy absorbed (MJ),  $R_T$  is the material destroyed ( $m^3$ ),  $A$  is the area of the tear area ( $m^2$ ),  $h$  is the height of the broken or heavily deformed longitudinal member (m),  $t_s$  is the thickness of the member (cm),  $C_{1.5} = 1.112 - 1.156\theta + 3.760\theta^2$ ,  $\theta$  is the half angle of the slice (rad),  $\sigma_0$  is the yield stress of the material (MPa),  $l$  is the cut length (m), and  $t_{eq}$  is the equivalent plate thickness (m) [31].

Each of the given equations incorporates many characteristics that describe the complexity of structural behaviour under impact, offering a framework for estimating the energy absorbed during a ship collision. The volume of material destroyed and the energy absorbed are directly correlated, according to Equation 1. The linear coefficient in this equation illustrates the proportionality of the relationship between the amount of energy dissipated during a collision and the quantity of volumetric damage. This knowledge is extended by Equation 2, which adds the damaged surface's size as a parameter indicating that ripping or rupture at the surface level significantly increases energy absorbed. This equation provides a more thorough viewpoint because it considers surface area failure and volumetric destruction. The computation is further improved by Equation 3, which considers the longitudinal structural members' thickness and height. The equation captures individual members' contributions to the absorbed energy, with special attention to their geometrical characteristics and structural importance. Lastly, a material-centric method for predicting energy absorption is offered by Equation 4. The length of the cut or tear, the equivalent plate thickness, and the material's yield stress are used to compute the energy.

## 2.2 Stiffened plate panel

In ship collisions, structural damage is a common consequence of the impact [32]. The stiffened plate panel forms a fundamental component of the ship's structure, representing the single-panel configurations of the ship's sides and bottom and the outer panels in double-side shell and double-bottom structures [33]. Widely utilized in ship construction, stiffened plate panels provide essential structural support to the hull, serving as the building blocks of the entire hull assembly, including the double bottom, side shells, and deck areas [34-36].

Composed of elementary plate panels and reinforced by ordinary stiffeners, these panels are enclosed by primary structural members, making them the core structural unit of a ship's hull. However, they are particularly vulnerable to damage during collisions with external objects. To ensure the structural safety of ships, it is critical to assess the load capacity that stiffened plate panels can withstand. Additionally, predictions regarding potential accident scenarios, the extent of damage, and the residual strength after sustaining impact-related damage are essential. They must be integrated into the stiffened plate panel design and manufacturing process [10,37,38]. When subjected to collision forces, stiffened plate panels may experience various damage types, including plate tension, cutting, folding, and intersection denting [31]. These damage mechanisms

underscore the importance of robust design methodologies and accurate predictive modelling to improve the resilience of ship structures under extreme conditions.

### 3. Crashworthiness analysis

#### 3.1 Crashworthiness definition & parameter

Crashworthiness involves the study of the plastic deformation of structures [12]. During a crash, the energy-absorbing structure of a vehicle absorbs its kinetic energy through plastic deformation, significantly reducing the mechanical impact on the vehicle and its occupants [11]. The main goal of crashworthiness studies is to protect individuals involved in impacts and collisions [12]. Ship collisions often cause severe damage to the hull structure and can result in loss of life, making crashworthiness a critical focus for the maritime industry. This focus aims to enhance the crashworthiness performance of hull structures to ensure crew safety. Generally, crashworthiness reflects the improved capacity of systems to withstand impact loads. In the context of ship-to-ship collisions, crashworthiness refers to the enhanced ability of the struck ship to absorb kinetic energy before the hull sustains damage [39].

Crashworthiness parameters consist of energy absorbed, specific energy absorbed, maximum crush force, and crush force efficiency [40,41]. Energy absorption ( $EA$ ) is determined by multiplying the crushing force by the displacement. The simulation results are presented as a force-displacement graph, where the shaded area under this curve represents the total energy absorbed, as calculated using Eq. 5:

$$EA = \int_0^s F_m dx, 0 < x < s \quad (5)$$

where  $F_m$  is the mean crushing force, and  $s$  is the final length of the crushing structure.

Moreover, the mean crushing force ( $F_m$ ), the average force over the structure's deformation, can be calculated using Eq. 6:

$$F_m = \frac{EA}{s_{max}} \quad (6)$$

where  $s_{max}$  is the maximum length of the crushing structure or deformed structure.

### 4. Benchmark and validation

The experimental reference profile in this study is an experimental test conducted by Alsos et al. [17]. Experimental testing was performed with quasi-static conditions by penetrating components as an indenter on the hull structure. Quasi-static analysis methods are often used and justified in engineering practice when quasi-static methods can capture the main characteristics of the structure response under low-velocity impact. The hull structure is modelled using a stiffened plate panel, a key component of the ship's hull. The experimental reference geometry includes both the indenter and the stiffened plate panel using a previous experiment conducted by Alsos et al. [17]. The indenter is milled out from a solid piece of steel. It has a cone shape with a spherical nose. The indenter is shaped like a cone with a spherical edge, featuring a radius of 200 mm from the centre of the cone's base and an angle of  $45^\circ$  between the base and the cone's surface. The plate measures 720 x 1200 mm with a thickness of 5 mm, the stiffener is 120 x 1200 mm with a thickness of 6 mm, and the frame is constructed from rectangular hollow section (RHS) steel, measuring 300 x 200 mm with a thickness of 12.5 mm. The experimental reference geometry and dimensions are illustrated in Fig. 1.

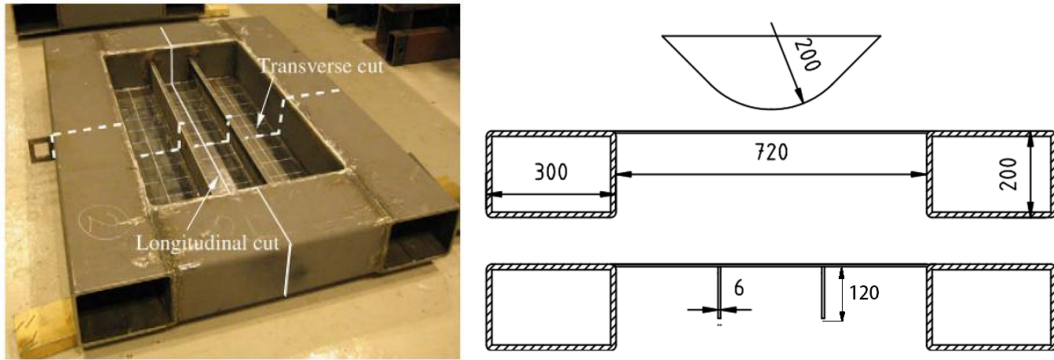


**Fig. 1** Structural geometry and dimension of Alsos et al. [17] stiffened plate panel experimental testing

The stiffened plate panel comprises two components: the plate and ordinary stiffeners. Each component is made from different grades of steel. The frame is constructed from high-strength steel (S355NH-EN10210), while the plate and stiffener are made from mild steel (S235JR-EN10025). The engineering stress-strain curve for the plate and stiffener materials can be seen in Fig. 2 and is detailed in Alsos et al. [17].

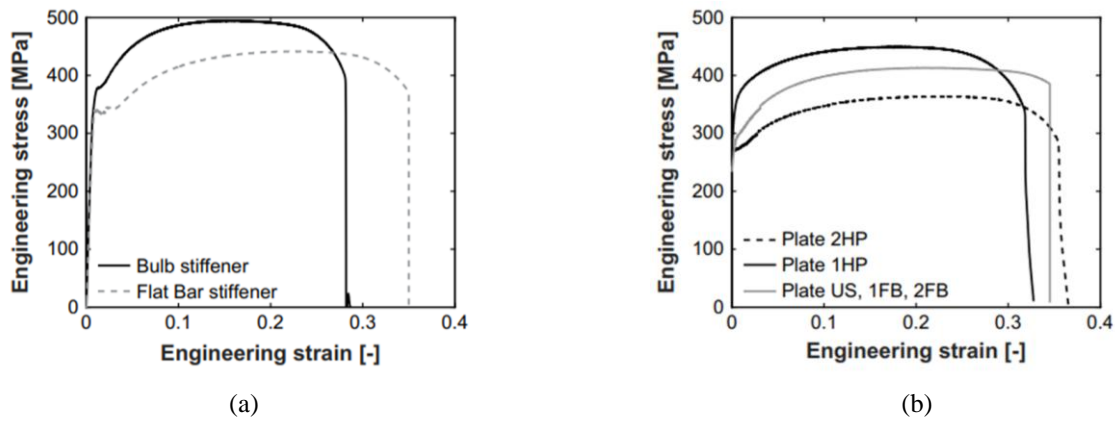


**Fig. 2** Material engineering stress-strain curve [17]: (a) stiffener, (b) plate

Experimental testing is carried out by penetrating the stiffened plate panel using an indenter mounted on a hydraulic jack. The hydraulic jack used has a maximum capacity of 250 tons. The indenter penetrates the stiffened plate panel with a controlled displacement of 0.167 mm/s. The displacement of the indenter was also measured using a displacement transducer placed on the ground. The experimental testing process is shown in Fig. 3.

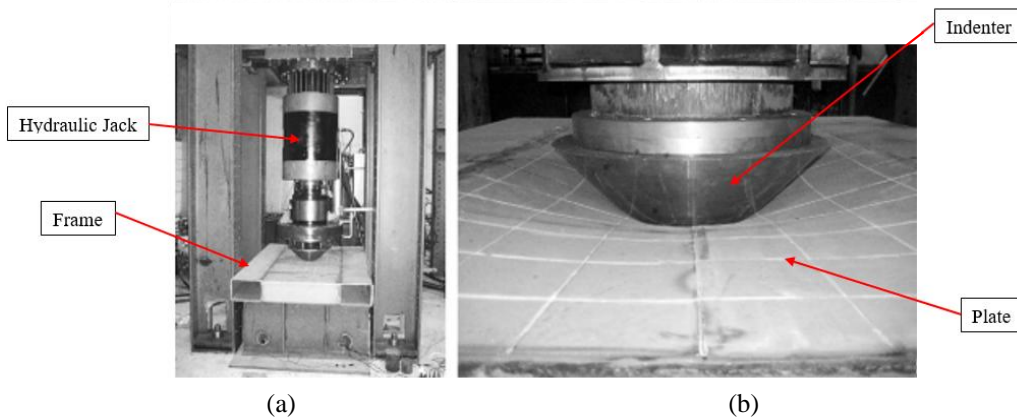


**Fig. 3** Alsos et al. [17] experimental test: (a) test setup, and (b) penetration of stiffened plate panel by the indenter

The validation procedure involves benchmarking against experimental test data as a reference. Simulation testing was conducted using finite element method analysis with ANSYS LS-Dyna software. In this simulation, each component of the stiffened plate panel and indenter structure was modelled using shell

elements with Belytschko-Lin-Tsay formulation, and each shell element included five integration points through its thickness. The mesh size for each component was set to 10 mm. The simulation employed two types of contact: automatic single-surface contact and automatic surface-to-surface contact. Automatic single-surface contact was used for each part of the stiffened plate panel to prevent self-penetration during progressive buckling. When the plate and stiffener are progressively buckled, contact between the plate and stiffener is possible, which is ideal for crashworthiness applications. Automatic surface-to-surface contact defined interactions between different component surfaces, such as between the indenter and the stiffened plate panel, and is suited for interactions involving rigid components. Simulation testing was carried out with quasi-static conditions. The movement of the indenter when penetrating the stiffened plate panel is set with a controlled displacement of 167 mm/s, 1000 times faster than the experiment (0.167 mm/s) due to limitations on computer resources and computational time. However, it is still in a quasi-static condition because if the load application is slower than 2000 mm/s, there is no significant inertia effect [16]. The final time of simulation testing, or call termination time, is set at 1.44 s so that the indenter will penetrate the stiffened plate panel as far as 240 mm. The speed of the indenter when penetrating is always constant so that there is no effect of acceleration or deceleration during penetration.

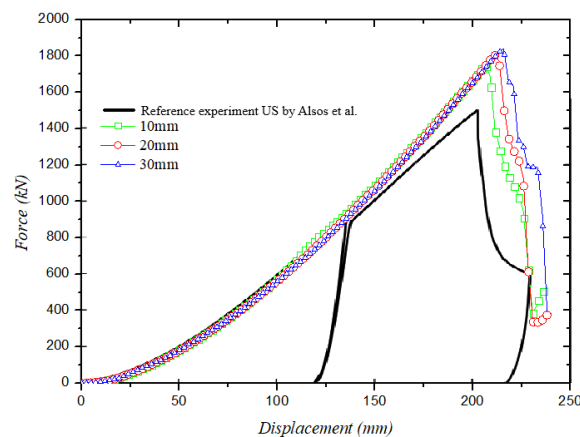


**Fig. 4** Force-displacement between numerical and experimental test of unstiffened (US) structure

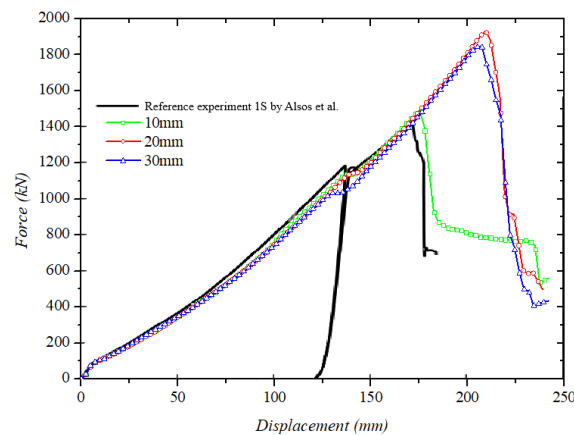


**Fig. 5** Force-displacement between numerical and experimental test of single stiffened (1S) structure

The validity of the simulation testing is evaluated by analyzing the force-displacement graphs obtained from the simulation and comparing them with those from experimental testing. Figures 4-6 depict these comparisons across three structural types: Unstiffened (US), Single Stiffened (1S), and Double Stiffened (2S). The results of the US and 2S structures show a gradual increase in force from the start of loading until the initial fracture occurs. In contrast, the 1S structure exhibits a sharp increase in force at the beginning of loading, followed by a slower rise to the initial fracture point. Following the initial fracture, there is a decrease in force values for all structures; however, the decrease is more pronounced in the US and 1S structures than in the 2S structure, which shows only a slight reduction. The comparative analysis further reveals that simulations using a 10mm mesh size more closely replicate the experimental results, including the peak force and initial fracture points, compared to simulations with 20mm and 30mm mesh sizes. This analysis confirms that the simulation

testing can accurately predict the fracture behaviour of stiffened plate panels, demonstrating the effectiveness of using a 10mm mesh size for these simulations.

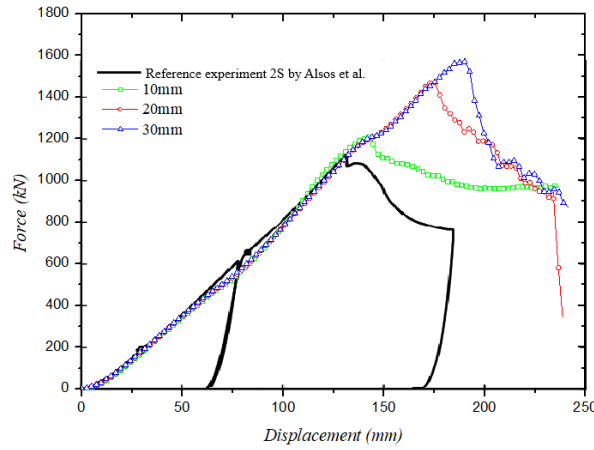


**Fig. 6** Force-displacement between numerical and experimental test of double stiffened (2S) structure

### 5. Parametric study

#### 5.1 Finite element modelling and setup

The model geometry represents a 1:3 scale of the dimensions found in medium-sized tankers, as stated in Alsos et al. [17]. The dimensions of the stiffened plate panel and the impactor stated in Table 1 in the simulation are based on experimental data.

**Table 1** Structural dimension of stiffened plate panel and indenter

Cross section	Cross section view	Dimensions (mm)
Tranverse cross section		$RI = 200$ $A = 5$ $B = 12.5$ $C = 120$ $D = 6$ $E = 720$ $F = 1320$
Longitudinal cross section		$SI = 135^\circ$ $H = 200$ $I = 1200$ $J = 1800$ $G = 300$

The geometry of the impactor component is modelled with an indenter. The structural geometry and adjustment of the solid geometry in the experiment to the shell geometry in the simulation test are shown in Fig. 7. The adjustment is made by defining the thickness of each component.

The material model selection during simulation is intended to select a material model that follows the material used in experimental testing, the loading conditions on the material, and the material structure response that occurs due to loading. The stiffened plate panel material is assumed to have isotropic plastic properties. It is modeled using the J2 plane stress flow theory, where the nominal stress-strain curve of the material is based on the engineering stress-strain curve shown in Fig. 2. Modifying the power law formulation involving plate strain presents the equivalent stress-strain curve, as shown in Eq 7:

$$a\sigma_{eq} = \begin{cases} \sigma_Y & \text{if } \epsilon_{eq} \leq \epsilon_{plat} \\ K (\epsilon_{eq} + \epsilon_0)^n & \end{cases} \quad (7)$$

where  $\sigma_{eq}$  is the quasi-static equivalent flow stress,  $\epsilon_{eq}$  is the quasi-static equivalent flow strain,  $\epsilon_{plat}$  is the equivalent plastic strain at plateau exit, and  $\sigma_y$  is the initial yield stress. Strain  $\epsilon_0$  allows the plateau and power law to intersect at  $(\epsilon_{plat}, \sigma_y)$ , obtained by Eq 8:

$$a\epsilon_0 = \left(\frac{\sigma_y}{K}\right)^{\frac{1}{n}} - \epsilon_{plat} \tag{8}$$

where  $K$  and  $n$  are the parameters of the material. Modified power law yield correlates well with the material's engineering stress-strain curve in Fig. 2, as reported by Alsos et al. [15]. ANSYS software uses the MAT\_003\_plastic kinematic material model for components in the stiffened plate panel, and the indenter material uses the MAT\_020\_rigid material model. The mechanical properties of the material are shown in Table 2.

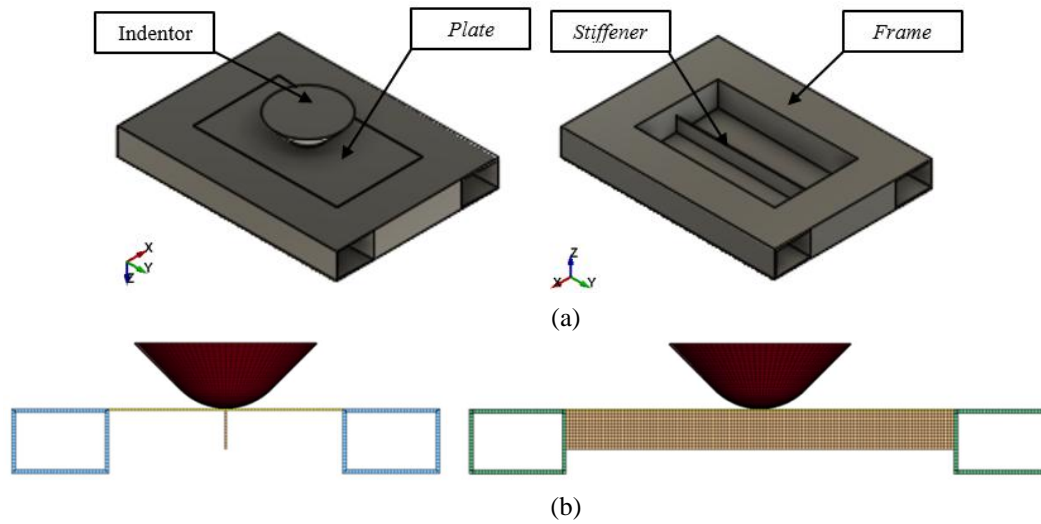


Fig. 7 (a) structural geometries of stiffened plate panel and impactor, (b) shell geometry adjustment

Table 2 Mechanical properties of stiffened plate panel structure material

Part	Material Grade	$\rho$ (kg/m <sup>3</sup> )	$\sigma_y$ (MPa)	$E$ (GPa)	$K$ (MPa)	$n$	$\epsilon_{plat}$	$\epsilon_f$	$\nu$
Plate	S235JR-EN10025	7850	285	210	740	0.24	-	0.35	0.3
Stiffener	S235JR-EN10025	7850	340	210	760	0.225	0.015	0.35	0.3
Frame	S355NH-EN10210	7850	390	210	830	0.18	0.01	0.28	0.3

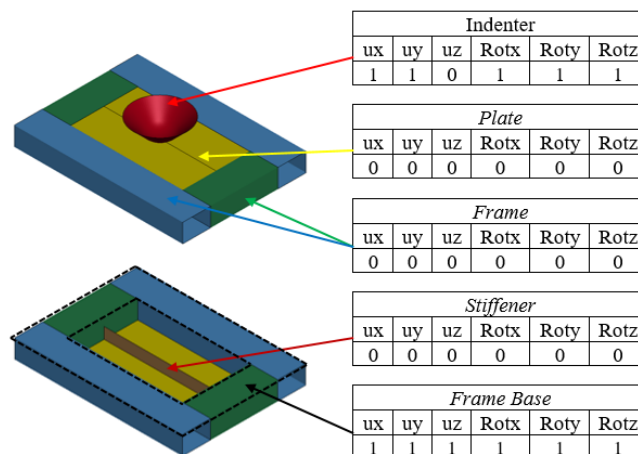


Fig. 8. Schematic loading condition and boundary conditions

The impact loading scheme begins with the indenter penetrating the stiffened plate panel along the Z axis at a constant speed of 167 mm/s. The indenter is constrained with fixed boundary conditions for all rotational motions along the X, Y, and Z axes. For translational motion, the indenter has fixed boundary conditions only along the X and Y axes. The model components have free boundary conditions for all

translational and rotational motions along the  $X$ ,  $Y$ , and  $Z$  axes. The base of the frame is assumed to be fixed in all degrees of freedom, with translational and rotational motions along the  $X$ ,  $Y$ , and  $Z$  axes constrained. The boundary conditions and loading schemes for both the indenter and the stiffened plate panel are illustrated in Fig. 8.

## 5.2 Design variation of stiffeners

The study examines scenario variations through both numerical and physical parameters. Numerical parameter variations include changes in mesh size, which are aimed at assessing how mesh size affects the accuracy of simulation results using the finite element method. Physical parameter variations involve stiffener types, spacing, and configuration changes. Fig. 9 shows 10 models with mesh variations in the range of 10-100 mm.

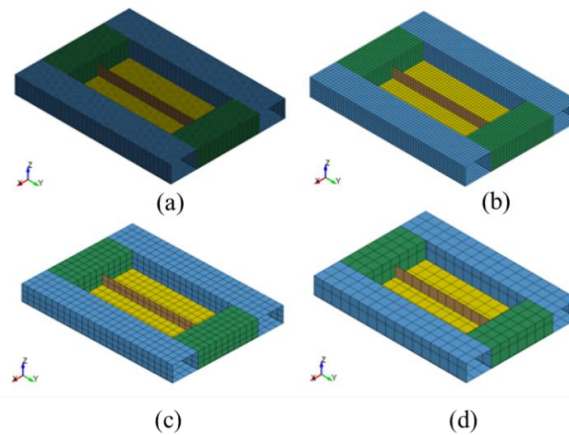


**Fig. 9** Mesh size variation geometry: (a) 10 mm, (b) 30 mm, (c) 70 mm, (d) 100 mm

In the second variation, the variation of stiffener type is analyzed to determine its effect on the crashworthiness performance of the stiffened plate panel when subjected to impact load. There are four stiffener types: Type I, Type L, Type T, and Type Y, each varied with two geometries: single stiffener and cross stiffener, as seen in Figs. 10 and 11. Each stiffener type maintains a fixed volume of  $1.334 \times 10^6 \text{ mm}^3$ , with the variation existing solely in the stiffener's shape.

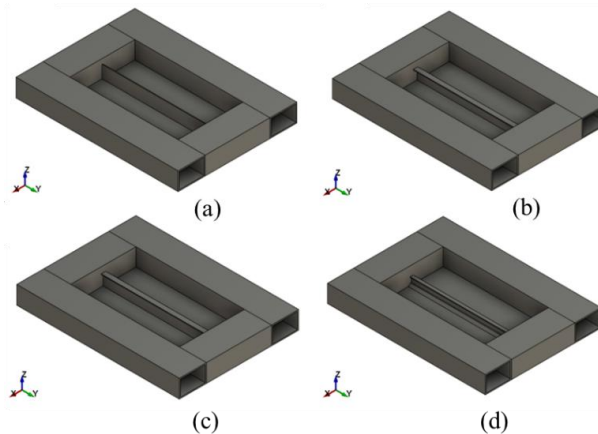


**Fig. 10** Single stiffener type geometry: (a) Single-I, (b) Single-L, (c) Single-T, (d) Single-Y

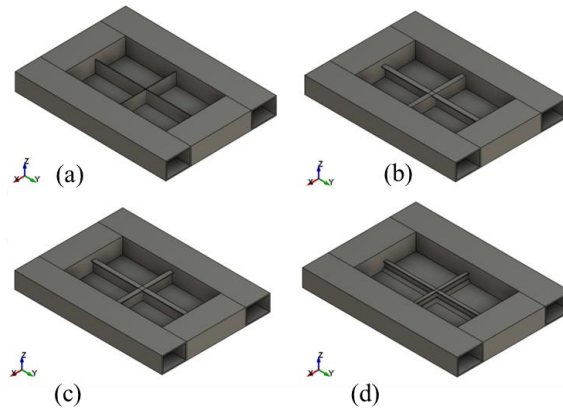


**Fig. 11** Cross stiffener type geometry: (a) Cross-I, (b) Cross-L, (c) Cross-T, (d) Cross-Y

The variation of stiffener spacing is studied to determine its effect on the stiffener Type Y crashworthiness performance when subjected to impact loads. There are four stiffener spacing: Spacing 1 is 360 mm apart, Spacing 2 is 240 mm apart, Spacing 3 is 180 mm apart, and Spacing 4 is 144 mm apart, as seen in Fig. 12. When the stiffener spacing is closer, the number of stiffeners in the structure will increase.

In the last variation scenario, four stiffener configurations were developed such as Config. 1 (single cross stiffener), Config. 2 (double cross stiffener), Config. 3 (double longitudinal stiffener), and Config. 4 (double transverse stiffener). The stiffeners in these configurations cross each other, and the stiffener spacing between two transverse stiffeners is 400 mm, while the stiffener spacing between two longitudinal stiffeners is 240 mm, as seen in Fig. 13.

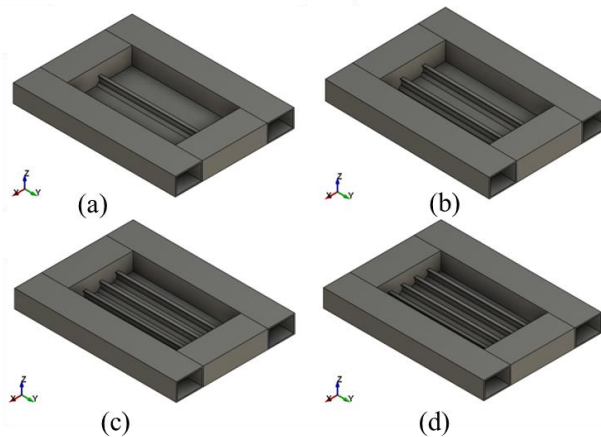


**Fig. 12** Geometry of stiffener spacings: (a) Spacing 1, (b) Spacing 2, (c) Spacing 3, (d) Spacing 4

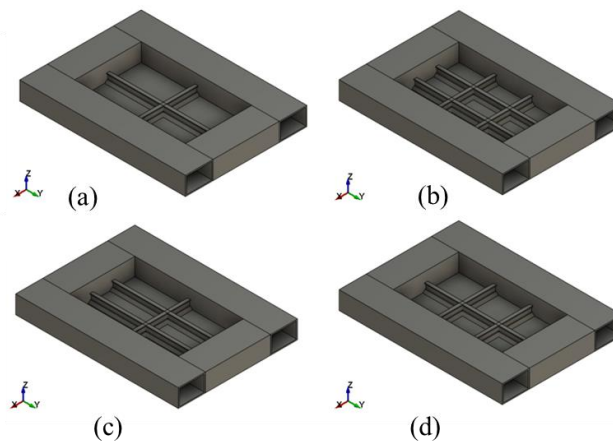
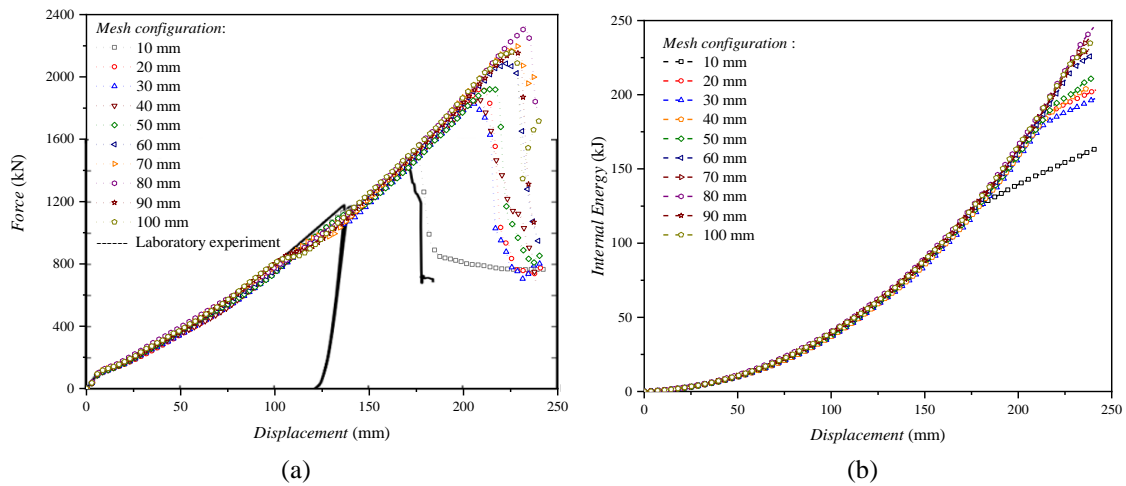


**Fig. 13** Geometry of stiffener configuration: (a) Config. 1, (b) Config. 2, (c) Config. 3, (d) Config. 4

## 6. Result and discussion

### 6.1 Comparison of crashworthiness performance on mesh size variations

This study examines the impact of mesh size on the accuracy of simulation results by testing various mesh size variations ranging from 10 to 100 mm using a validated stiffened plate panel geometry. The accuracy is assessed through force-displacement curves, internal energy, and deformation contours, as seen in Fig. 14. Results indicate that smaller mesh sizes yield more accurate simulations, with the 10 mm mesh size showing the closest match to experimental data. It exhibited a 6.6 % deviation in peak force and a 3.16 % difference in initial fracture displacement. Larger mesh sizes delayed the onset of initial fracture, leading to over-predictions in peak force and increased fracture displacement values. Based on force-displacement data, internal energy graphs from Fig. 14b exhibit consistent trends across all mesh sizes, showing energy increasing until the point of initial fracture. However, larger mesh sizes lead to excessively high internal energy levels due to delayed fractures and overestimating peak forces. The 10 mm mesh size offers the most accurate correlation with experimental results, proving its effectiveness for precise modelling. It demonstrates that the 10 mm mesh size is most suitable for achieving reliable and accurate simulations.



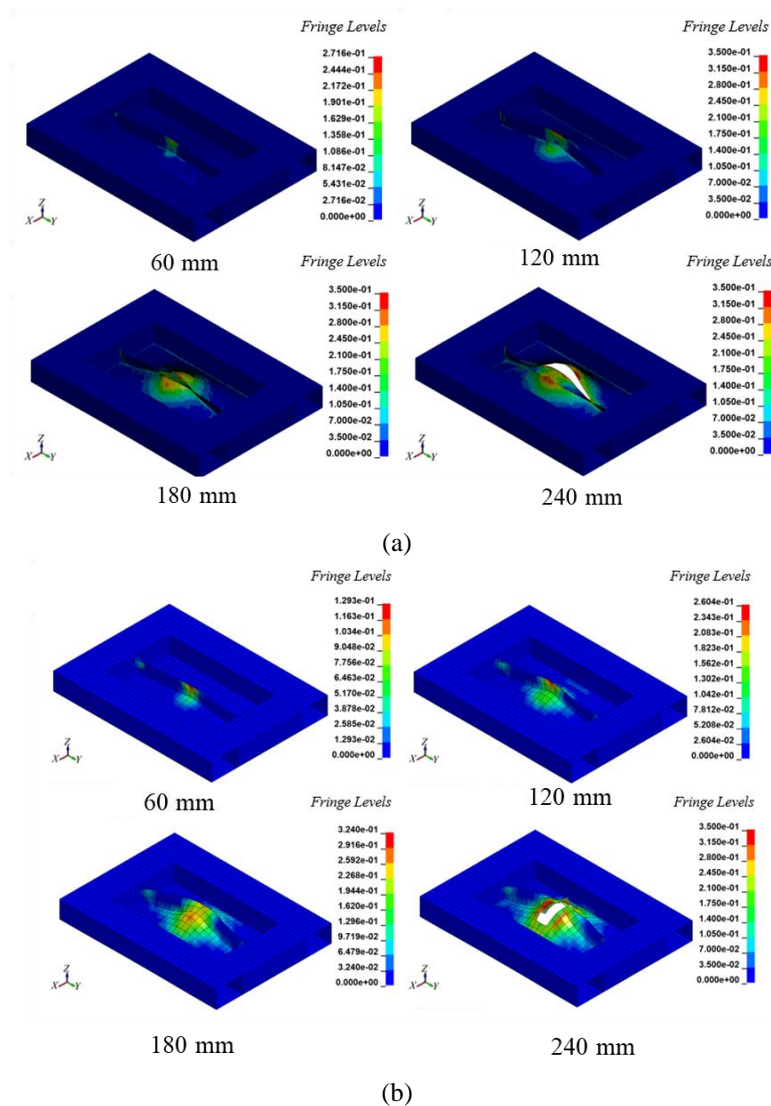
**Fig. 14** Simulation result under mesh size variation, a) force-displacement graph, b) internal energy.

Table 3 illustrates that while fracture energy values increase with mesh size, the 10 mm mesh size achieves the highest accuracy, exhibiting only a 2.88 % relative error compared to experimental results. Conversely, larger mesh sizes show significantly greater errors; for example, the 80 mm mesh registers a 97.63 % relative error. This data indicates a clear positive correlation between mesh size and error magnitude: larger mesh sizes lead to decreased simulation accuracy. Consequently, the 10 mm mesh size is optimal as it minimizes error and ensures the most reliable simulation outcomes.

**Table 3** Comparison of fracture energy and error percentage on mesh size variation

Mesh Size	Fracture Energy (kJ)	Error (%)
10	121.4	2.88
20	176.1	49.22
30	165.8	40.49
40	167.9	42.25
50	189.2	60.3
60	207.4	75.74
70	221.5	87.69
80	233.2	97.63
90	219.5	85.98
100	217.9	84.68

Fig. 15 displays the effective plastic strain contours for 10 mm and 50 mm mesh sizes, highlighting areas of high strain in red. The 10 mm mesh accurately concentrates high strain at the intersection of the plate and stiffener, where initial fractures occur, aligning with experimental results from Alsos et al. [17]. In contrast, the 50 mm mesh presents a more dispersed strain distribution throughout the plate and stiffener without clear localization at their intersection, resulting in inaccurate fracture patterns and less resemblance to experimental findings. These observations underscore that larger mesh sizes compromise simulation accuracy by affecting deformation contours and fracture behaviour. However, the 10 mm mesh size maintains the highest accuracy, as corroborated by force-displacement graphs, fracture energy values, and deformation contours, closely matching the experimental data.



**Fig. 15** Effective plastic strain contours at various displacements (a) (a) Mesh size 10 mm, (b) Mesh size 50 mm

### 6.2 Comparison of crashworthiness performance on stiffener type variation

The stiffened plate panel incorporates four types of stiffeners: I, L, T, and Y. Additionally, two geometric configurations are applied: single stiffener and cross stiffener geometries. Crashworthiness of these configurations can be evaluated using force-displacement graphs and internal energy values, depicted in Fig. 16. Fig. 16a shows the force-displacement graphs for each single stiffener type, revealing similar patterns across the stiffener types at the start of penetration. Specifically, the Single-I, Single-L, and Single-T types exhibit a significant increase in force early on.

As penetration progresses, the force in each type continues to rise until reaching a peak, indicating the onset of an initial fracture. Following this peak, there is a significant drop in force as the fracture advances.

Notably, the force-displacement graphs for the Single-I and Single-T types maintain a horizontal trajectory even after initial fracturing, suggesting no decrease in force despite ongoing structural damage. This horizontal pattern is attributed to the folding of stiffeners at specific displacements: 145 mm for the Single-I and 103 mm for the Single-T. Among these, the Single-L stiffener demonstrates the best performance, achieving the highest peak force (1992.62 kN) and the longest displacement before initial fracture (207.85 mm), indicative of superior ductility and energy absorption. In contrast, the Single-I stiffener shows the poorest results, with the lowest peak force (1348.44 kN) and shortest initial fracture displacement (158.87 mm), reflecting greater stiffness before fracture.

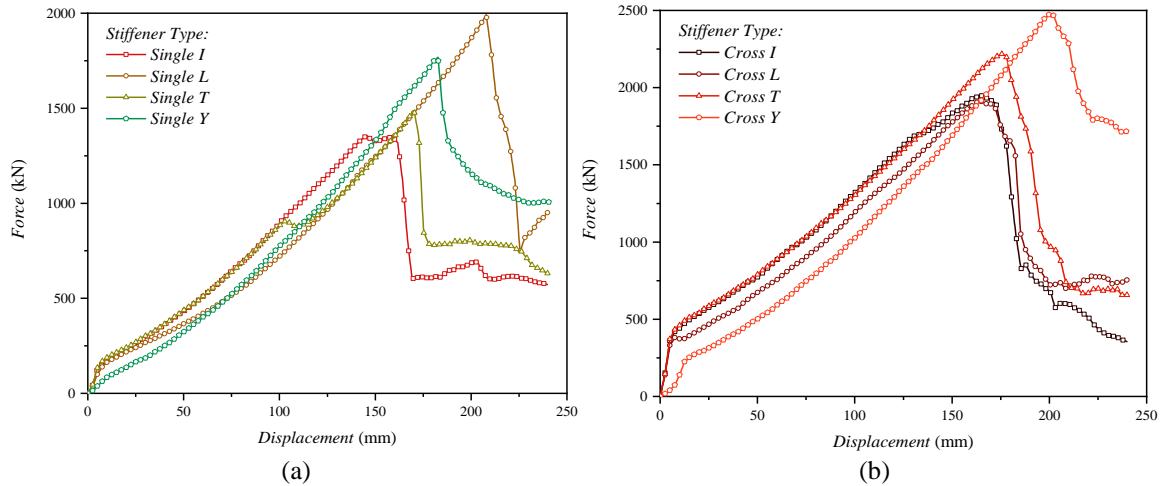


**Fig. 16** Force-displacement graph on stiffener type variation: a) single stiffener geometry, a) cross stiffener geometry

As shown in Fig. 16b, the force-displacement graph of the cross stiffener geometry exhibits a similar pattern. At the onset of penetration, the force value of each structure rises sharply, with the Cross-T type experiencing the most significant increase among all types. The Cross-Y type outperforms other types in both peak force and initial fracture displacement, indicating superior resistance to fracture and higher energy absorption capacity. In contrast, the Cross-L type has the lowest peak force and initial fracture displacement, showing poor performance under impact loading. The Cross-I and Cross-T types exhibit greater stiffness before fracturing, as evidenced by higher force values before the initial fracture than the Cross-L and Cross-Y types. Specifically, the Cross-Y type exhibits the highest peak force at 2474.18 kN and the longest initial fracture displacement at 201.93 mm, underscoring its excellent performance. Conversely, the Cross-L type has the lowest peak force at 1910.39 kN and the shortest initial fracture displacement at 164.91 mm. The Cross-I type, while similar to the Cross-L in peak force and displacement, demonstrates slightly better strength before initial fracture. Overall, these results highlight that cross-stiffener geometry significantly influences the structural properties of stiffened plates, particularly their flexural behaviour.

The internal energy graphs for single and cross stiffener geometries, as shown in Figures 17a and 17b, respectively, exhibit notable trends. In the single stiffener configuration, each stiffener type-Single-I, Single-T, Single-L, and Single-Y, shows a significant increase in internal energy from the start of penetration until the initial fracture occurs. Following this, the slope of the graphs flattens as force resistance decreases due to structural damage. Single-I and Single-T have nearly identical internal energy values at the displacement just before the initial fracture, as do Single-L and Single-Y. In the cross-stiffener configuration, similar patterns are observed where internal energy significantly rises to the point of initial fracture and then becomes more gradual. The Cross-I, Cross-L, and Cross-T types exhibit a similar post-fracture slope, indicating decreased force resistance. The Cross-Y type maintains a consistent increase in internal energy up to a displacement of 240 mm. Additionally, before the initial fracture, Cross-I and Cross-T types show higher internal energy values than Cross-L and Cross-Y, reflecting variations in their structural responses to penetration and damage.

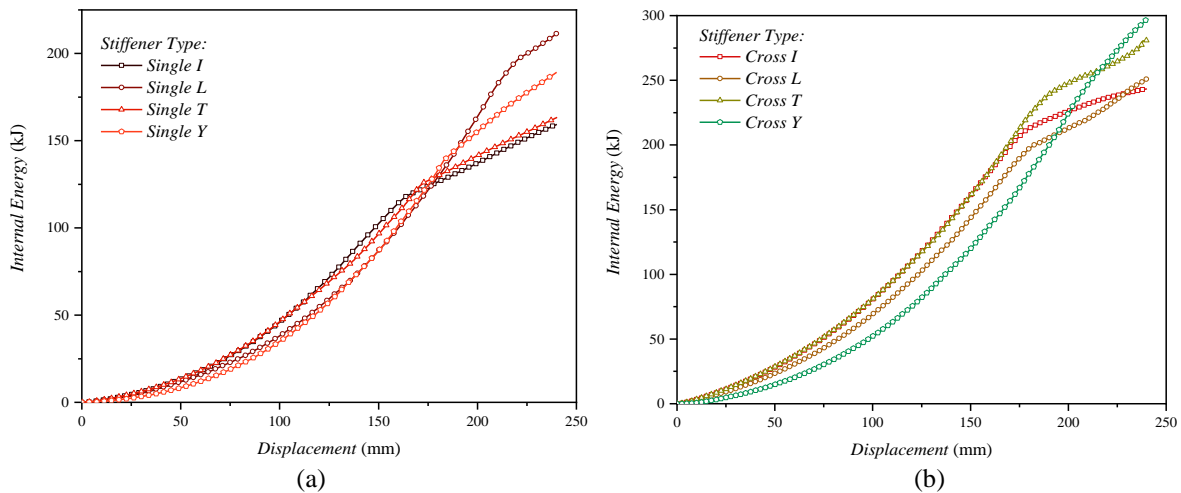


**Fig. 17** Internal energy on various stiffener types: (a) single stiffener geometry, (b) cross stiffener geometry

Fig. 18 shows the effective plastic strain contours for the different types of stiffeners with single stiffener geometry. The effective plastic strain measures the deformation of the material due to the applied load. The more effective the plastic strain, the more likely the material will fail. The Single-I, Single-T, and Single-Y types have plastic strain concentrations at the intersection between the plate and stiffener components. The Single-L type has a plastic strain concentration on the plate component close to the intersection between the plate and the stiffener component. The effective plastic strain contours are colour-coded, with red representing the highest and blue representing the lowest values. The concentration of stress and strain contained in the structure will indicate the location or point of initial fracture. Fractures will occur in areas with a high stress concentration and plastic strain. The fracture in Single-I, Single-L, and Single-T types is tearing at the intersection area between the plate and stiffener components. Meanwhile, tearing occurs in the plate component close to the intersection area in the Single-L type. In addition, folding occurs in the stiffener component in the Single-I, Single-L, and Single-T types.

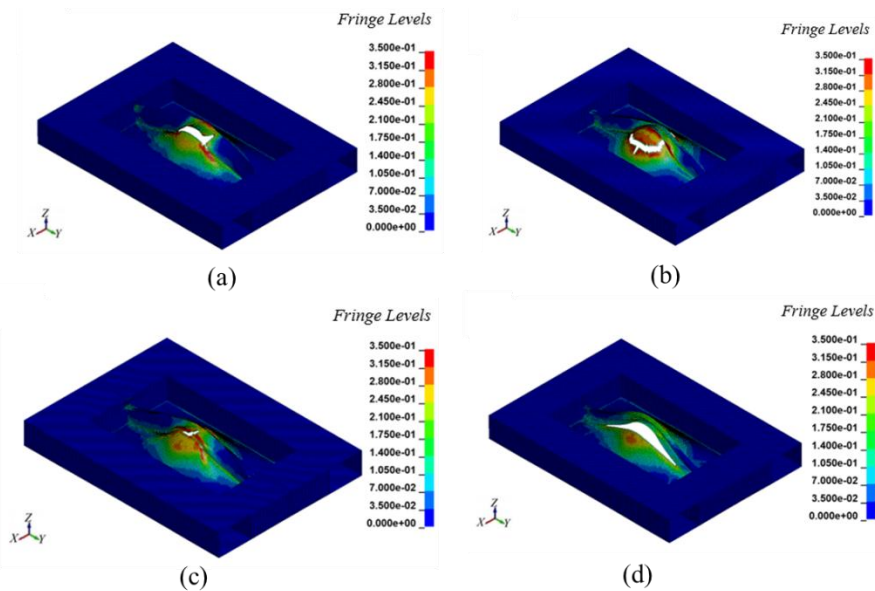


**Fig. 18** Effective plastic strain contours at displacement 240 mm: a) Single-I type, b) Single-L type, c) Single-T type, d) Single-Y type

Fig. 19 depicts the variation of effective plastic strain for different types of stiffeners with cross-shaped geometry. The effective plastic strain measures the permanent deformation of a material due to loading. The Cross-I, Cross-L, Cross-T, and Cross-Y types have plastic strain concentrations at the intersection between the plate and stiffener components. The concentration of stress and strain contained in the structure will indicate the location or point of initial fracture. Fractures will occur in areas with high plastic stress and strain concentrations. The fracture type in the Cross-I, Cross-L, Cross-T, and Cross-Y types is tearing at the

intersection area between the plate and stiffener components. In the Cross-I type, tearing also occurs in the stiffener component, namely in the intersection area between stiffener components. In the Cross-L and Cross-T types, intersection denting also occurs at the intersection area of the stiffener components.

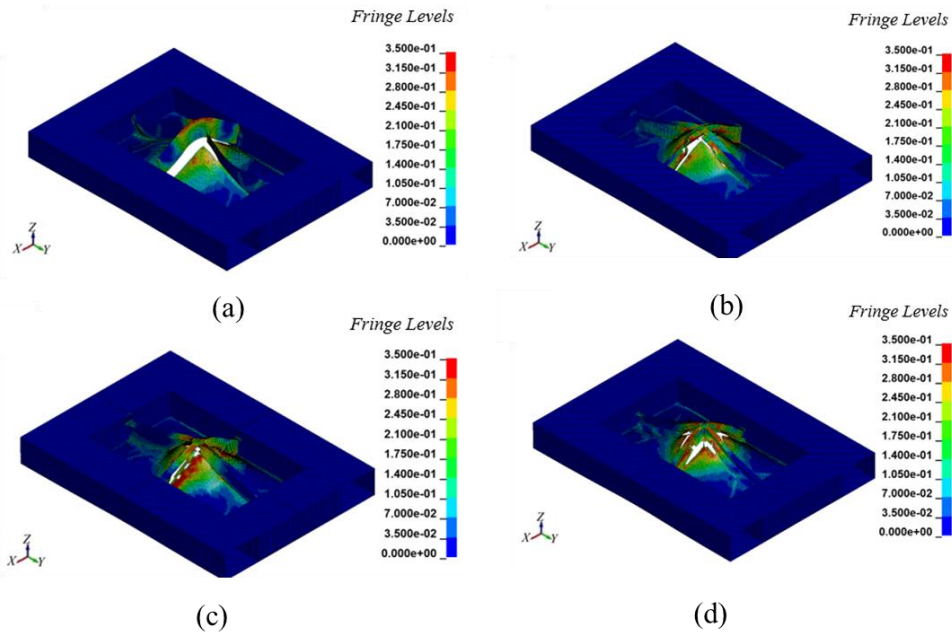


**Fig. 19** Effective plastic strain contours at displacement 240 mm: a) Cross-I type, b) Cross-L type, c) Cross-T type, d) Cross-Y type

### 6.3 Comparison of crashworthiness performance on stiffener spacing variation

The Y-stiffened plate panel features four different stiffener spacings: Spacing 1 (360 mm), Spacing 2 (240 mm), Spacing 3 (180 mm), and Spacing 4 (144 mm), as shown in Fig. 20a. The force-displacement graphs indicate that decreasing stiffener spacing generally enhances crashworthiness. After an initial fracture, the force in Spacing 1 drops significantly, whereas in Spacings 2, 3, and 4, the reduction in force is minimal, maintaining a relatively horizontal graph. It indicates that the force values in Spacings 2, 3, and 4 remain consistent despite ongoing structural fractures. Spacing 3 and 4 exhibits a higher force value before the initial fracture than the other types.

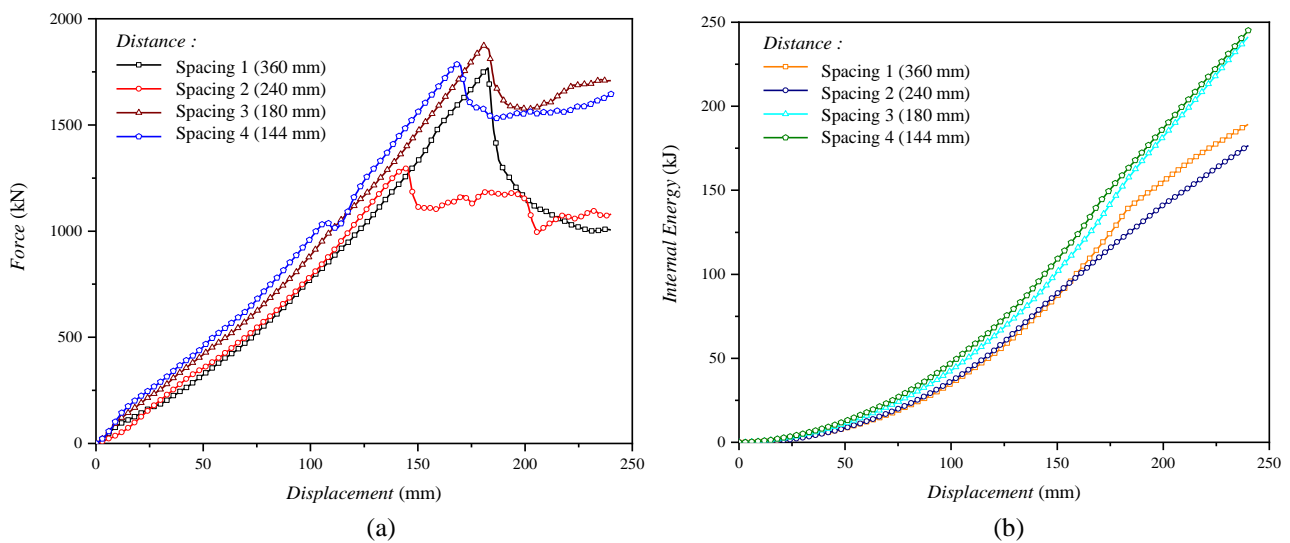


**Fig. 20** Simulation result under stiffener spacing variations: a) force-displacement graph, b) internal energy

Fig. 20b illustrates the internal energy trends across these spacings, showing a substantial increase up to the point of initial fracture, followed by a sloping rise as the structure's force resistance decreases. Spacing 1 experiences a pronounced sloping increase in internal energy post-fracture. Conversely, Spacings 2, 3, and 4

4 display similar trends in internal energy throughout the penetration up to a displacement of 240 mm. Among these, Spacing 3 and 4 have the highest internal energy value before the fracture occurs, highlighting differences in energy absorption capabilities among the spacings.

Fig. 21 shows the contours of effective plastic strain at variations in stiffener spacing. Spacing 1, 2, and 4 types have plastic strain concentrations at the intersection between the plate and the stiffener component. In contrast, the Spacing 3 type has a plastic strain concentration on the plate component close to the intersection between the plate and the stiffener. High concentration is shown in red on the effective plastic strain contour. The stress and strain concentration contained in the structure will indicate the location or point of initial fracture. Fractures will occur in areas with a high stress concentration and plastic strain. The fracture in the Spacing 1, Spacing 2, and Spacing 4 types is tearing at the intersection area between the plate and stiffener components. In the Spacing 3 type, tearing occurs on the plate component close to the intersection area between the plate component and the stiffener. In addition, tearing in the Spacing 2 type also occurs in the plate component.

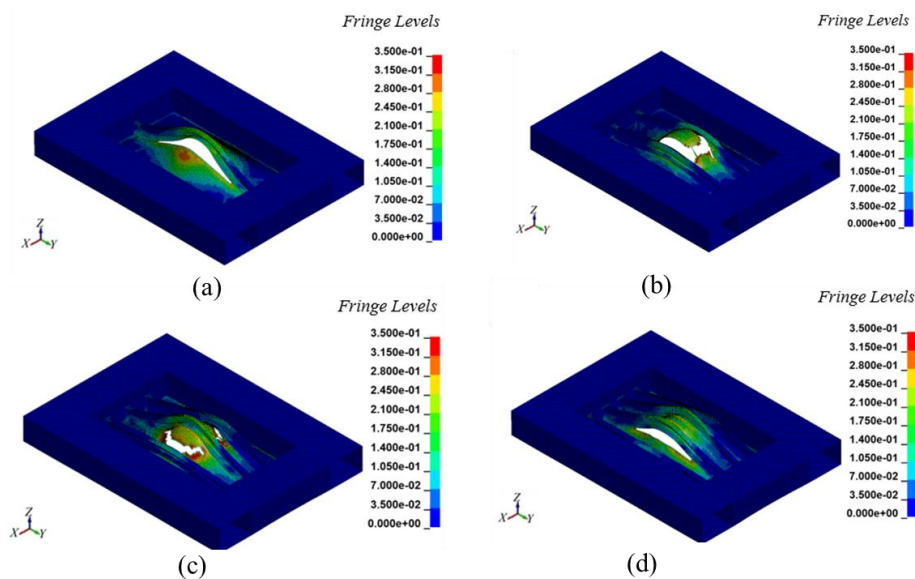


**Fig. 21** Effective plastic strain contours at displacement 240 mm: a) Spacing 1, b) Spacing 2, c) Spacing 3, d) Spacing 4

#### 6.4 Comparison of crashworthiness performance on stiffener configuration variations

The stiffened plate panel features four different stiffener configurations using the Y stiffener type: Config. 1 (single cross stiffener), Config. 2 (double cross stiffener), Config. 3 (double longitudinal stiffener), and Config. 4 (double transverse stiffener). Fig. 22a displays the force-displacement graphs for these configurations, which are similar in shape across all types. Post-initial fracture, the force values decrease across configurations, with notable differences. In Config. 2, after a slight decrease following the initial fracture, the force value rises again, peaking at a displacement of 203 mm, indicating continued force increase despite ongoing structural damage. Conversely, Config. 3 exhibits a relatively horizontal force-displacement graph post-fracture, suggesting that the force value remains constant despite continued fracturing, and this configuration shows higher force values before the initial fracture compared to other configurations. Fig. 22b details the internal energy trends, showing a significant increase up to the initial fracture point for all configurations, followed by a more gradual rise as the structures' force resistance decreases. Config. 2 maintains a consistent internal energy increase up to a displacement of 240 mm. Config. 3, however, displays the highest internal energy values before the initial fracture among all configurations, reflecting its enhanced energy absorption capabilities.

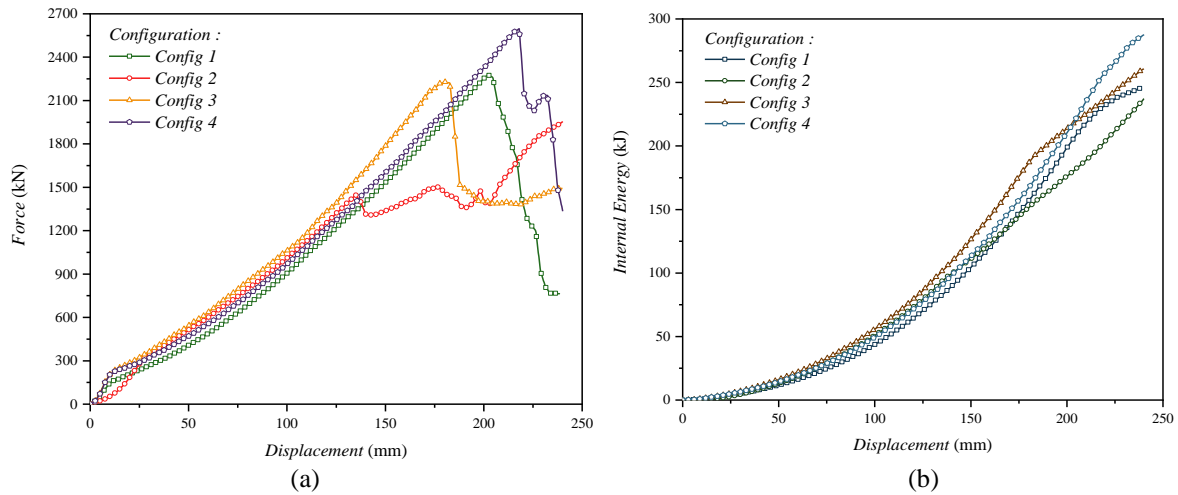


**Fig. 22** Simulation result under stiffener configuration variations: a) force-displacement graph, b) internal energy

Fig. 23 shows the contours of the effective plastic strain on the stiffener configuration variation. Structures of Config. 1, Config. 2, and Config. 4 types have a plastic strain concentration at the intersection between the plate and the stiffener component. In comparison, the Config. 3 type has a plastic strain concentration on the plate component close to the intersection between the plate and the stiffener. The high concentration is shown in red on the effective plastic strain contour.

The concentration of stress and strain contained in the structure will indicate the location or point of initial fracture. Fractures will occur in areas with a high stress concentration and plastic strain. The fracture types in the Config. 1, Config. 2, and Config. 4 type structures are tearing at the intersection area between the plate and stiffener components. In the Config. 3 type, tearing occurs on the plate component close to the intersection between the plate and the stiffener component. In addition, tearing in the Config. 3 types also occur in the stiffener component.

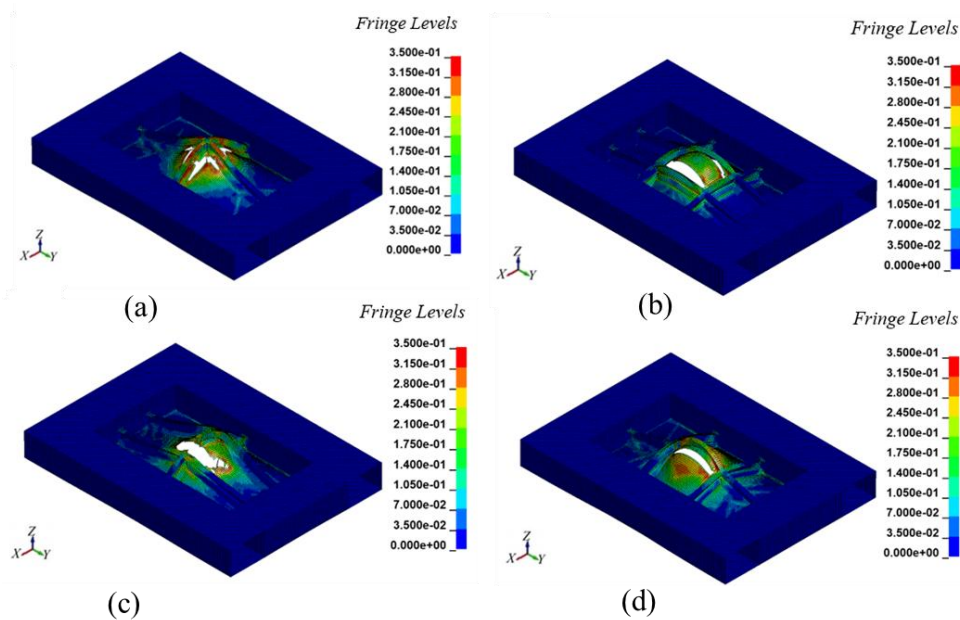


**Fig. 23** Effective plastic strain contours at displacement 240 mm: a) Config. 1, b) Config. 2, c) Config. 3, d) Config. 4

## 7. Conclusions

The impact loading of stiffened plate panels has been investigated using quasi-static numerical simulations with ANSYS software, focusing on numerical parameters (mesh size) and geometric parameters (stiffener type, stiffener spacing, and stiffener configuration). The findings demonstrate a high level of

accuracy in the benchmarking study, where simulation results align closely with experimental data. The force-displacement trends closely match the experimental results, with differences in peak force resistance and initial fracture displacement values being less than 5 %. Similarly, the discrepancy in fracture energy values between simulation and experimental results is below 5 %. Moreover, the deformation and fracture contours from the simulations are consistent with experimental observations, showing tearing predominantly at the intersection between the plate and stiffener components.

The analysis highlights the importance of mesh size in determining simulation accuracy. A fine mesh size of 10 mm produces the most accurate results, whereas larger mesh sizes, such as 80 mm, significantly compromise accuracy by introducing greater error values. It underscores the necessity of selecting an appropriate mesh size to ensure reliable simulation outcomes. The study identifies variations among stiffener types, spacing, and configurations regarding crashworthiness performance. The Single-L type demonstrates the highest crashworthiness performance among single stiffener geometries, while the Single-I type exhibits the lowest. The Cross-Y type outperforms others for cross-stiffened structures, while the Cross-I type shows the lowest performance. Stiffener spacing also plays a crucial role, with decreasing spacing yielding superior crashworthiness performance. Similarly, stiffener configuration also impacts performance.

This research underscores the significance of studying ship structural crashworthiness in collision scenarios, given the substantial risks of material loss, environmental harm, and potential loss of life. Future studies could further develop this field by incorporating environmental conditions (e.g., corrosion and temperature effects) or considering the impact of weld geometry, material heterogeneity, and residual stresses from fabrication. Including these factors would allow for a more realistic and comprehensive assessment of structural crashworthiness, ultimately improving the safety and resilience of ship designs under impact conditions.

### Acknowledgement

This work was supported by the Institute for Research and Community Services (LPPM) Universitas Diponegoro, under the Research Scheme of Riset Kolaborasi Indonesia (RKI) 2024, with a research grant/contract no. 442-03/UN7.D2/PP/IV/2024. The authors gratefully acknowledge the support.

### REFERENCES

- [1] Chen, J., Bian, W., Wan, Z., Yang, Z., Zheng, H., Wang, P. 2019. Identifying factors influencing total-loss marine accidents in the world: Analysis and evaluation based on ship types and sea regions. *Ocean Engineering*, 191, 106495. <https://doi.org/10.1016/j.oceaneng.2019.106495>
- [2] Ugurlu, H., Cicek, I. 2022. Analysis and assessment of ship collision accidents using Fault Tree and Multiple Correspondence Analysis. *Ocean Engineering*, 245, 110514. <https://doi.org/10.1016/j.oceaneng.2021.110514>
- [3] Jon, M. H., Kim, Y. P., Choe, U. 2021. Determination of a safety criterion via risk assessment of marine accidents based on a Markov model with five states and MCMC simulation and on three risk factors. *Ocean Engineering*, 236, 109000. <https://doi.org/10.1016/j.oceaneng.2021.109000>
- [4] Wang, H., Liu, Z., Wang, X., Graham, T., Wang, J. 2021. An analysis of factors affecting the severity of marine accidents. *Reliability Engineering and System Safety*, 210, 107513. <https://doi.org/10.1016/j.ress.2021.107513>
- [5] Wang, L., Huang, R., Shi, W., Zhang, C. 2021. Domino effect in marine accidents: Evidence from temporal association rules. *Transport Policy*, 103, 236–244. <https://doi.org/10.1016/j.tranpol.2021.02.006>
- [6] Rong, H., Teixeira, A. P., Soares, C. G. 2022. Ship collision avoidance behaviour recognition and analysis based on AIS data. *Ocean Engineering*, 245, 110479. <https://doi.org/10.1016/j.oceaneng.2021.110479>
- [7] Calle, M. A. G., Oshiro, R. E., Alves, M. 2017. Ship collision and grounding: Scaled experiments and numerical analysis. *International Journal of Impact Engineering*, 103, 195–210. <https://doi.org/10.1016/j.ijimpeng.2017.01.021>
- [8] Tian, W., Ma, Q., Zhang, J., Meng, B., Gan, Z., Wan, H., He, Y. 2020. Ship collision risk assessment model for qinzhou port based on event sequence diagram. *Brodogradnja*, 71(2), 1-14. <https://doi.org/10.21278/brod71201>
- [9] Ali, T., Peng, Y., Jinhao, Z., Kun, L., Renchuan, Y. 2022. Crashworthiness optimization method for sandwich plate structure under impact loading. *Ocean Engineering*, 250, 110870. <https://doi.org/10.1016/j.oceaneng.2022.110870>
- [10] Gao, J., Zhang, Y. 2024. Ship collision avoidance decision-making research in coastal waters considering uncertainty of target ships. *Brodogradnja*, 75 (2), 1-16. <https://doi.org/10.21278/brod75203>

- [11] Gong, C., Bai, Z., Wang, Y., Zhang, L. 2021. On the crashworthiness performance of novel hierarchical multi-cell tubes under axial loading. *International Journal of Mechanical Sciences*, 206, 106599. <https://doi.org/10.1016/j.ijmecsci.2021.106599>
- [12] Abdullah, N. A. Z., Sani, M. S. M., Salwani, M. S., Husain, N. A. 2020. A review on crashworthiness studies of crash box structure. *Thin-Walled Structures*, 153, 106795. <https://doi.org/10.1016/j.tws.2020.106795>
- [13] Gonzales, M. A. C., Kujala, P. 2021. Additive manufacturing of miniature marine structures for crashworthiness verification: A numerical revision. *Applied Ocean Research*, 111, 102653. <https://doi.org/10.1016/j.apor.2021.102653>
- [14] Kitarović, S., Žanić, V., Andrić, J. 2013. Progressive Collapse Analyses of Stiffened Box- Girders Submitted to Pure Bending. *Brodogradnja*, 64 (4), 439-455.
- [15] Alsos, H. S., Amdahl, J., Hopperstad, O. S. 2009. On the resistance to penetration of stiffened plates, Part II: Numerical analysis. *International Journal of Impact Engineering*, 36(7), 875–887. <https://doi.org/10.1016/j.ijimpeng.2008.11.004>
- [16] Abubakar, A., Dow, R. S. 2013. Simulation of ship grounding damage using the finite element method. *International Journal of Solids and Structures*, 50(5), 623–636. <https://doi.org/10.1016/j.ijsolstr.2012.10.016>
- [17] Alsos, H. S., Amdahl, J. 2009. On the resistance to penetration of stiffened plates, Part I - Experiments. *International Journal of Impact Engineering*, 36(6), 799–807. <https://doi.org/10.1016/j.ijimpeng.2008.10.005>
- [18] Paik, J. K. 2007. Practical techniques for finite element modeling to simulate structural crashworthiness in ship collisions and grounding (Part I: Theory). *Ships Offshore Structures*, 2(1), 69–80. <https://doi.org/10.1533/saos.2006.0148>
- [19] Kõrgesaar, M., Tabri, K., Naar, H., Reinhold, E. 2014. Ship collision simulations using different fracture criteria and mesh size. In *International Conference on Offshore Mechanics and Arctic Engineering*, Vol. 45424, p. V04AT02A045, American Society of Mechanical Engineers. <https://doi.org/10.1115/OMAE2014-23576>
- [20] Kõrgesaar, M., Romanoff, J. 2014. Influence of mesh size, stress triaxiality and damage induced softening on ductile fracture of large-scale shell structures. *Marine Structures*, 38, 1-17. <https://doi.org/10.1016/j.marstruc.2014.05.001>
- [21] Ringsberg, J. W., Amdahl, J., Chen, B. Q., Cho, S. R., Ehlers, S., Hu, Z., et al. 2018. MARSTRUCT benchmark study on nonlinear FE simulation of an experiment of an indenter impact with a ship side-shell structure. *Marine Structures*, 59, 142-157. <https://doi.org/10.1016/j.marstruc.2018.01.010>
- [22] Romanoff, J., Korgesaar, M., Lehto, P., Berntsson, K., Remes, H. 2022. Experimental Investigations on Stiffened and Web-core Sandwich Panels Made for Steel under Quasi-Static Penetration. *Procedia Structural Integrity*, 37, 17-24. <https://doi.org/10.1016/j.prostr.2022.01.055>
- [23] Bulatović, S., Aleksić, V., Milović, Lj., Zečević, B. 2021. An analysis of impact testing of high strength low-alloy steels used in ship construction. *Brodogradnja*, 72 (3), 1-12. <https://doi.org/10.21278/brod72301>
- [24] Güzel, B., Korkmaz, F.C. 2020. Reducing water entry impact loads on marine structures by surface modification. *Brodogradnja*, 71 (1), 1-18. <https://doi.org/10.21278/brod71101>
- [25] Prabowo, A. R., Bae, D. M., Sohn, J. M., Zakki, A. F., Cao, B., Cho, J. H. 2017. Effects of the rebounding of a striking ship on structural crashworthiness during ship-ship collision. *Thin-Walled Structures*, 115, 225–239. <https://doi.org/10.1016/j.tws.2017.02.022>
- [26] Prabowo, A. R., Baek, S. J., Byeon, J. H., Bae, D. M., Cho, J. H., Sohn, J. M. 2017. Investigation on the Structural Damage of a Double-Hull Ship, Part I - Ship Collision. *Procedia Structural Integrity*, 5, 935–942. <https://doi.org/10.1016/j.prostr.2017.07.126>
- [27] Prabowo, A. R., Nubli, H., Sohn, J. M. 2020. Energy dissipation of ship structures subjected to impact loading: A study case in side collision. *Procedia Structural Integrity*, 27, 171–178. <https://doi.org/10.1016/j.prostr.2020.07.023>
- [28] Bai, Y., Jin, W.-L. 2016. Ship Collision and Grounding. In *Marine Structural Design* (pp. 459–473). Elsevier. <https://doi.org/10.1016/B978-0-08-099997-5.00023-X>
- [29] Prabowo, A. R., Bae, D. M., Sohn, J. M., Zakki, A. F., Cao, B., Wang, Q. 2017. Analysis of structural behaviour during collision event accounting for bow and side structure interaction. *Theoretical and Applied Mechanics Letters*, 7(1), 6–12. <https://doi.org/10.1016/j.taml.2016.12.001>
- [30] Zhang, S., Pedersen, P. T., Villavicencio, R. 2019. External dynamics of ship collisions and grounding. In *Probability and Mechanics of Ship Collision and Grounding*, 62-146. <https://doi.org/10.1016/B978-0-12-815022-1.00002-5>
- [31] Zhang, S. 1999. The Mechanics of Ship Collisions. *Ocean Engineering Journal - Department of Naval Architecture and Offshore Engineering - Technical University of Denmark*, January, 1–185.
- [32] Liu, B., Villavicencio, R., Pedersen, P. T., Guedes Soares, C. 2021. Analysis of structural crashworthiness of double-hull ships in collision and grounding. *Marine Structures*, 76, 102898. <https://doi.org/10.1016/j.marstruc.2020.102898>
- [33] Liu, B., Pedersen, P. T., Zhu, L., Zhang, S. 2018. Review of experiments and calculation procedures for ship collision and grounding damage. *Marine Structures*, 59, 105–121. <https://doi.org/10.1016/j.marstruc.2018.01.008>
- [34] Shama, M., 2013. Buckling of Stiffened Panels. In *Buckling of Ship Structures* (pp. 267–304). Springer Berlin Heidelberg. [https://doi.org/10.1007/978-3-642-17961-7\\_11](https://doi.org/10.1007/978-3-642-17961-7_11)

- [35] Platypodis, E. L., Anyfantis, K. N. 2022. On the Modeling of Ship Stiffened Panels Subjected to Uniform Pressure Loads. *Applied Mechanics*, 3(1), 125–143. <https://doi.org/10.3390/applmech3010010>
- [36] Jiao, J., Chen, Z., Xu, S. 2024. CFD-FEM simulation of water entry of aluminium flat stiffened plate structure considering the effects of hydroelasticity. *Brodogradnja*, 75(1), 1-28. <https://doi.org/10.21278/brod75108>
- [37] Xu, M. C., Song, Z. J., Zhang, B. W., Pan, J. 2018. Empirical formula for predicting ultimate strength of stiffened panel of ship structure under combined longitudinal compression and lateral loads. *Ocean Engineering*, 162, 161–175. <https://doi.org/10.1016/j.oceaneng.2018.05.015>
- [38] Cho, S.-R., Lee, H.-S. 2009. Experimental and analytical investigations on the response of stiffened plates subjected to lateral collisions. *Marine Structures*, 22(1), 84–95. <https://doi.org/10.1016/j.marstruc.2008.06.003>
- [39] Klanac, A., Ehlers, S., Jelovica, J. 2009. Optimization of crashworthy marine structures. *Marine Structures*, 22(4), 670–690. <https://doi.org/10.1016/j.marstruc.2009.06.002>
- [40] Samer, F., Abed, A. A., Bassam, A. 2021. Crashworthiness enhancement of thin-walled hexagonal tubes under flexural loads by using different stiffener geometries. *Materials Today: Proceedings*, 42, 2887–2895. <https://doi.org/10.1016/j.matpr.2020.12.739>
- [41] Baisane, P., Sakle, N. 2023. Evaluation of crashworthiness parameters for foam-filled concentric tubes using explicit dynamics simulation. *Materials Today: Proceedings*, 72, 1224–1230. <https://doi.org/10.1016/j.matpr.2022.09.287>